

PREPARED FOR SUBMISSION TO JHEP

Complete $\mathcal{O}(\alpha_s^2)$ Corrections to the Leptonic Invariant Mass Spectrum in $b \rightarrow X_c l \bar{\nu}_l$ Decay

Mateusz Czaja,^a Mikołaj Misiak,^a Abdur Rehman^{b,c}

^a*Institute of Theoretical Physics, Faculty of Physics, University of Warsaw, 02-093 Warsaw, Poland.*

^b*Department of Physics, University of Alberta, Edmonton, AB T6G 2J1, Canada.*

^c*Department of Environmental and Physical Sciences, Faculty of Science, Concordia University of Edmonton, Alberta, T5B 4E4, Canada.*

E-mail: mp.czaja@uw.edu.pl, misiak@fuw.edu.pl, rehman3@ualberta.ca

ABSTRACT: In the determination of the Cabibbo-Kobayashi-Maskawa matrix element $|V_{cb}|$ from inclusive semileptonic B -meson decays, moments of the leptonic invariant mass spectrum constitute valuable observables. To evaluate them with sufficient precision, perturbative $\mathcal{O}(\alpha_s^2)$ corrections to the analogous spectrum in the partonic $b \rightarrow X_c l \bar{\nu}_l$ decay are necessary. In the present paper, we compute such perturbative corrections in a complete manner, including contributions from the triple-charm channel, namely from the $cc\bar{c}l\bar{\nu}_l$ final states. We present our results in terms of numerical fits in both the single- and triple-charm cases. We confirm the recently found results for the single-charm correction, and analyze the triple-charm channel impact on centralized moments of the spectrum.

Contents

1	Introduction	1
2	Details of the calculation	3
2.1	The q^2 -spectrum	3
2.2	The effective width formula	4
2.3	Calculation of the bare effective width	6
2.4	Renormalization	7
3	Results	8
3.1	The $b \rightarrow X_{3c} l \bar{\nu}_l$ spectrum	8
3.2	The $b \rightarrow X_{1c} l \bar{\nu}_l$ spectrum	9
3.3	Corrections to the q^2 -moments	11
4	Conclusions	13
A	Numerical values of fit parameters	15

1 Introduction

The Cabibbo-Kobayashi-Maskawa (CKM) matrix element $|V_{cb}|$ enters the Standard Model (SM) predictions for many phenomenologically important observables. The well-known examples are the $B_s \rightarrow \mu^+ \mu^-$ decay branching ratio or the neutral Kaon mixing parameter ϵ_K . The uncertainty of $|V_{cb}|$ determination in the SM limits the power of such observables in constraining parameter spaces of beyond-SM theories. Currently, around 50% of the theoretical uncertainty in both $\mathcal{B}(B_s \rightarrow \mu^+ \mu^-)$ [1] and $|\epsilon_K|$ [2] is due to $|V_{cb}|$, making it a crucial element at the high-luminosity frontier of particle physics.

The value of $|V_{cb}|$ is usually extracted from a fit to kinematic moments of spectra in the inclusive semileptonic $B \rightarrow X_c l \bar{\nu}_l$ decay, with $l = e, \mu$. Traditionally, either the charged lepton energy (E_l) or the hadronic invariant mass squared (r^2) spectra were used [3], as these were the only distributions initially measured at the B -factories (see, e.g., ref. [4]). The first measurements of the leptonic invariant mass squared (q^2) spectrum¹ by Belle [5] and Belle-II [6] opened a new chapter in the efforts to improve the precision of the SM prediction for $|V_{cb}|$.

A comprehensive introduction to the treatment of inclusive semileptonic B -meson decays in the Heavy Quark Expansion (HQE) formalism can be found in chapter 6 of ref. [7]. Both the decay rate and the above-mentioned kinematic moments of spectra can be evaluated in terms of a double power series in α_s and $\bar{\Lambda}/m_b$, where $\bar{\Lambda}$ is the dominant contribution

¹with low E_l removed via cuts on q^2 only

to the difference between the B -meson and b -quark masses, i.e. $\bar{\Lambda} \simeq m_B - m_b$. In the case of the decay rate (zeroth moment) $\Gamma_{sl} \equiv \Gamma(B \rightarrow X_c l \bar{\nu}_l)$, one finds²

$$\Gamma_{sl} = \Gamma_{sl}^{\text{part}} + \frac{G_F^2 m_b^5 |V_{cb}|^2}{192\pi^3} \sum_k \frac{C_k \langle O_k^{(n_k)} \rangle}{m_b^{n_k-3}}, \quad (1.1)$$

where the partonic rate $\Gamma_{sl}^{\text{part}} \equiv \Gamma(b \rightarrow X_c^{\text{part}} l \bar{\nu}_l)$ is the perturbatively calculable inclusive decay rate of a free b -quark into the lepton-antineutrino pair and any partonic state X_c^{part} . The dominant contribution to the r.h.s. of eq. (1.1) is given by $\Gamma_{sl}^{\text{part}}$. The remainder is a correction of order $(\bar{\Lambda}/m_b)^2$ that is parameterized by diagonal matrix elements (expectation values) of dimension- n_k local operators $O_k^{(n_k)}$ ($n_k \geq 5$) in the decaying B -meson state at rest. Explicit expressions for those operators up to dimension 6 can be found, e.g., in eqs. (8)-(11) of ref. [9]. The matrix elements $\langle O_k^{(n_k)} \rangle$ scale like $\bar{\Lambda}^{n_k-3}$, i.e.,

$$\langle O_k^{(n_k)} \rangle \equiv \frac{\langle B(\vec{p}=0) | O_k^{(n_k)}(x) | B(\vec{p}=0) \rangle}{2m_B} \sim \bar{\Lambda}^{n_k-3}, \quad (1.2)$$

under the standard normalization convention $\langle B(\vec{p}) | B(\vec{q}) \rangle = 2m_B (2\pi)^3 \delta^{(3)}(\vec{p} - \vec{q})$. Their x -independence is easily verified by writing $O_k^{(n_k)}(x) = e^{iPx} O_k^{(n_k)}(0) e^{-iPx}$, and then using the fact that $|B(\vec{p})\rangle$ is an eigenstate of the momentum operator P .

The structure of the local operators $O_k^{(n_k)}$ is obtained in the operator product expansion but values of their matrix elements are non-perturbative quantities that have to be extracted together with $|V_{cb}|$ in a fit to experimental data. The dimensionless Wilson coefficients C_k parameterize short-distance QCD effects. They are functions of $\frac{m_c}{m_b}$ only, and can be perturbatively determined, order-by-order in α_s .

Expressions analogous to eq. (1.1) hold for kinematic moments of spectra, too. Therefore, one can constrain the dominant matrix elements $\langle O_k^{(n_k)} \rangle$ by using experimental information on such moments. Moreover, as shown in ref. [10], certain sets of non-perturbative matrix elements come in fixed linear combinations in Reparametrization-Invariant (RPI) observables. Consequently, less operators need to be treated as independent. Up to $n_k = 6$, there are 4 generic operators, and 3 operators needed for RPI observables.³ Up to $n_k = 7$, these numbers are 13 and 8, respectively. A spectral moment is RPI provided the kinematic variables of the considered spectrum are independent of the B -meson four-velocity v . Moments of the q^2 spectrum are therefore RPI, while those in $E_l = vp_l$ or $r^2 = (m_B v - p_l - p_{\bar{\nu}_l})^2$ are not.

The experimental setups usually veto events with small E_l due to large backgrounds. On the theory side, removing $E_l < E_{\text{cut}}$ would break the RP invariance, necessitating the inclusion of all possible operators. Instead, one can remove the low E_l region with a lower cut on q^2 – see figure 6.2 of ref. [7]. The q^2 spectrum with a cut remains RPI, and preserves its simpler non-perturbative structure, simultaneously being compatible with the

² G_F denotes the Fermi constant measured in the muon decay [8]. Throughout the paper, we neglect non-leading corrections in α_{em} or $m_b/(\text{electroweak scale})$.

³Provided one neglects the $n_k = 6$ operators whose Wilson coefficients vanish at the tree level — see section 5 ref. [10].

experimental requirements. The first fits using the q^2 spectrum were already performed in refs. [11, 12].

To calculate moments of the q^2 spectrum with a cut, one needs to begin with the dominant, perturbative terms in the formulae that are analogous to eq. (1.1). At any given order in α_s , it is sufficient to determine $d\Gamma_{sl}^{\text{part}}/dq^2$, and then evaluate its moments with any experimentally desirable cut. Such a calculation has recently been completed up to $\mathcal{O}(\alpha_s^2)$ in ref. [13] without including numerically subdominant contributions from the triple-charm channel, namely from the $cc\bar{c}l\bar{\nu}_l$ final states.

In the present work, we complete the calculation of the $\mathcal{O}(\alpha_s^2)$ correction to $d\Gamma_{sl}^{\text{part}}/dq^2$ by including the triple-charm contributions. We also independently confirm the single-charm results of ref. [13]. Our results are provided in terms of precise numerical fits for the spectrum as a function of q^2 , the charm quark mass m_c , and the renormalization scale μ at which the strong coupling constant is renormalized.

Let us note that corrections to $d\Gamma_{sl}/dq^2$ that are suppressed by $(\bar{\Lambda}/m_b)^2$ and $(\bar{\Lambda}/m_b)^3$ have already been determined up to $\mathcal{O}(\alpha_s^1)$ in refs. [9, 14, 15]. Moreover, both $\Gamma_{sl}^{\text{part}}$ and the first few moments of $d\Gamma_{sl}^{\text{part}}/dq^2$ without any cut are already known up to $\mathcal{O}(\alpha_s^3)$ from refs. [16] and [17], respectively. However, no moment measurements without cuts are available.

The article is organized as follows. In section 2, we discuss details of our calculation. In section 3, we present results for the $\mathcal{O}(\alpha_s^2)$ correction to $d\Gamma_{sl}^{\text{part}}/dq^2$ and its moments, with subsections 3.1 and 3.2 dedicated, respectively, to the triple-charm $b \rightarrow X_{3c} l\bar{\nu}_l$ and single-charm $b \rightarrow X_{1c} l\bar{\nu}_l$ channels, and subsection 3.3 describing the impact on q^2 moments. We conclude in section 4. Various numerical fit coefficients are collected in appendix A. In the ancillary file, we provide these fits in a `Mathematica`-readable format.

2 Details of the calculation

2.1 The q^2 -spectrum

In the standard first step of the calculation, all particles heavier than the b -quark are integrated out of the SM. As already mentioned, we work at the leading order in α_{em} and $m_b/(\text{electroweak scale})$. In such a case, one is left with a single effective operator, namely a Fermi-like interaction between the quark and lepton currents. The leptonic current contribution factorizes, and is fixed to all orders in α_s . Consequently, the unpolarized differential rate of the semileptonic b -quark decay can be written as

$$d\Gamma_{sl}^{\text{part}} = \frac{1}{2} \frac{1}{2m_b} dPS_{p_b \rightarrow p_l p_{\bar{\nu}_l} p_c \{p_X\}} \frac{1}{M_W^4} \left[\sum_X \sum_{\sigma_H} |\mathcal{M}_{b \rightarrow W^* c X}|^2 \right]_{\mu\nu} \left[\sum_{\sigma_l} |\mathcal{M}_{W^* \rightarrow l \bar{\nu}_l}|^2 \right]^{\mu\nu}. \quad (2.1)$$

Here, X stands for all the final-state partons except for the charm quark that gets produced in the b -quark annihilation vertex. As mentioned above, the matrix element factorizes into the hadronic and leptonic parts, denoted by $\mathcal{M}_{b \rightarrow W^* c X}$ and $\mathcal{M}_{W^* \rightarrow l \bar{\nu}_l}$ respectively, summed over the discrete degrees of freedom indexed with σ_H and σ_l . The phase space element can

be factorized as [18]

$$dPS_{p_b \rightarrow p_l p_{\bar{l}} p_c \{p_X\}} = \frac{1}{128\pi^4 m_b} dE_l dq^2 dr^2 dPS_{r \rightarrow p_c \{p_X\}}, \quad (2.2)$$

where $q \equiv p_l + p_{\bar{l}}$ and $r \equiv p_b - q$. Throughout this work, we treat l and \bar{l} as massless.

In the notation of eq. (2.1), the leptonic and partonic tensors are given by

$$g_{ew}^2 L_{\mu\nu} \equiv \left[\sum_{\sigma_l} |\mathcal{M}_{W^* \rightarrow l \bar{l}}|^2 \right]_{\mu\nu}, \quad (2.3)$$

$$g_{ew}^2 |V_{cb}|^2 W_{\mu\nu} \equiv \int dPS_{r \rightarrow p_c \{p_X\}} \left[\sum_X \sum_{\sigma_H} |\mathcal{M}_{b \rightarrow W^* c X}|^2 \right]_{\mu\nu},$$

where g_{ew} is the electroweak $SU(2)$ gauge coupling. Combining eqs. (2.1)–(2.3), we obtain

$$\frac{d\Gamma_{sl}^{\text{part}}}{dq^2 dr^2} = \frac{G_F^2 |V_{cb}|^2}{16\pi^4 m_b^2} W_{\mu\nu} \int_{E_-}^{E_+} dE_l L^{\mu\nu}, \quad (2.4)$$

where $E_{\pm} \equiv (q^0 \pm |\vec{q}|)/2$ are the kinematical bounds on the lepton energy E_l in the decaying b -quark rest frame, for fixed q^2 and r^2 .

The leptonic tensor can be evaluated in a straightforward manner. It reads

$$L^{\mu\nu} \equiv p_l^\mu p_{\bar{l}}^\nu - (p_l p_{\bar{l}}) g^{\mu\nu} + p_{\bar{l}}^\mu p_l^\nu - i \epsilon^{\mu\nu\rho\sigma} (p_l)_\rho (p_{\bar{l}})_\sigma. \quad (2.5)$$

The partonic tensor can be decomposed into Lorentz structures as

$$W^{\mu\nu} = -W_1(q^2, r^2) g^{\mu\nu} + W_2(q^2, r^2) \frac{p_b^\mu p_b^\nu}{m_b^2} + (\text{other}), \quad (2.6)$$

where the omitted possible terms vanish when contracted with the E_l integral of $L_{\mu\nu}$ in the limit of massless leptons. Combining the above two equations allows for a straightforward integration on the r.h.s. of eq. (2.4), yielding

$$\frac{d\Gamma_{sl}^{\text{part}}}{dq^2} = \frac{G_F^2 |V_{cb}|^2}{16\pi^4 m_b^2} \int dr^2 |\vec{q}| \left(W_1 q^2 + \frac{W_2}{3} |\vec{q}|^2 \right). \quad (2.7)$$

2.2 The effective width formula

The r.h.s. of eq. (2.7) is reminiscent of the top-quark decay rate or, more generally, decay rate $\tilde{\Gamma}$ of a massive fermion into a lighter fermion and a massive vector boson with four-momentum q , mediated by a left-handed fermion current. To derive a relation between $\tilde{\Gamma}$ and $d\Gamma_{sl}^{\text{part}}/dq^2$, we can consider the SM with parameters tuned to retain the physical values of quark masses, CKM-matrix elements and G_F , but with the W -boson mass set to $\sqrt{q^2}$. In other words, we can consider the SM with so small electroweak gauge couplings that the W boson is lighter than the b quark, and $\tilde{\Gamma} = \Gamma(b \rightarrow X_c W)$. To facilitate the use of the optical theorem, we choose the unitary gauge for the light W -bosons. Such a choice removes

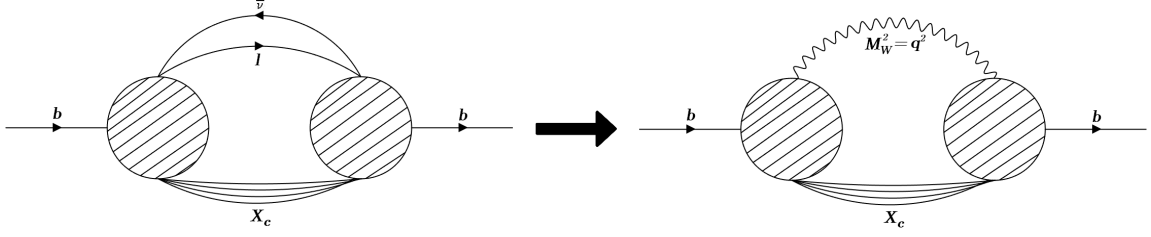


Figure 1: Diagrammatic depiction of the replacement of the lepton pair by an auxiliary vector boson.

all contributions of would-be Goldstone bosons from the amplitude. As before, we decouple all particles heavier than the b quark, and neglect non-leading electroweak corrections.

Let p_b , p_c , and $\{p_X\}$ be defined as in the previous subsection, while q now stands for the final-state W -boson momentum in $b \rightarrow X_c W$. The differential phase-space element of this process can be decomposed as

$$dPS_{p_b \rightarrow p_c q p_X} = \frac{dr^2}{2\pi} dPS_{p_b \rightarrow q r} dPS_{r \rightarrow p_c \{p_X\}}. \quad (2.8)$$

The two body volume $dPS_{p_b \rightarrow q r}$ for fixed q^2 and r^2 is constant and reads

$$dPS_{p_b \rightarrow q r} = \frac{1}{16\pi^2} \frac{|\vec{q}|}{m_b} d\Phi_q, \quad (2.9)$$

where Φ_q is the angular direction of the W -boson. In the rest frame of the b -quark, the length $|\vec{q}|$ is fixed for given values of q^2 , r^2 , and m_b^2 . In this frame, the decay is also isotropic, so in the total width we can simply replace

$$dPS_{p_b \rightarrow q r} \rightarrow \frac{1}{4\pi} \frac{|\vec{q}|}{m_b}. \quad (2.10)$$

The unpolarized total rate of this process can now be written as

$$\tilde{\Gamma} = \frac{q^2 G_F \sqrt{2}}{m_b} \frac{|V_{cb}|^2}{8\pi^2 m_b} \int dr^2 |\vec{q}| W^{\mu\nu} \sum_{\rho} \varepsilon_{\mu}^{(\rho)*} \varepsilon_{\nu}^{(\rho)}, \quad (2.11)$$

where ρ indexes the final-state W -boson polarization, and $\varepsilon_{\mu}^{(\rho)}$ are the polarization vectors that satisfy

$$\sum_{\rho} \varepsilon_{\mu}^{(\rho)*} \varepsilon_{\nu}^{(\rho)} = -g_{\mu\nu} + \frac{q_{\mu} q_{\nu}}{q^2}. \quad (2.12)$$

In eq. (2.11), the $W^{\mu\nu}$ tensor is defined exactly as in eq. (2.3), because the non-leptonic part of each diagram is the same in the true-SM semileptonic decay and in the modified-SM $b \rightarrow X_c W$ decay. Using the polarization sum rule (2.12) and the decomposition⁴ (2.6) leads to the following effective width formula

$$\frac{d\Gamma_{sl}^{\text{part}}}{dq^2} = \frac{\sqrt{2} G_F}{12\pi^2} \tilde{\Gamma}. \quad (2.13)$$

⁴The omitted part on the r.h.s. of eq. (2.6) vanishes under contraction with the r.h.s. of eq. (2.12).

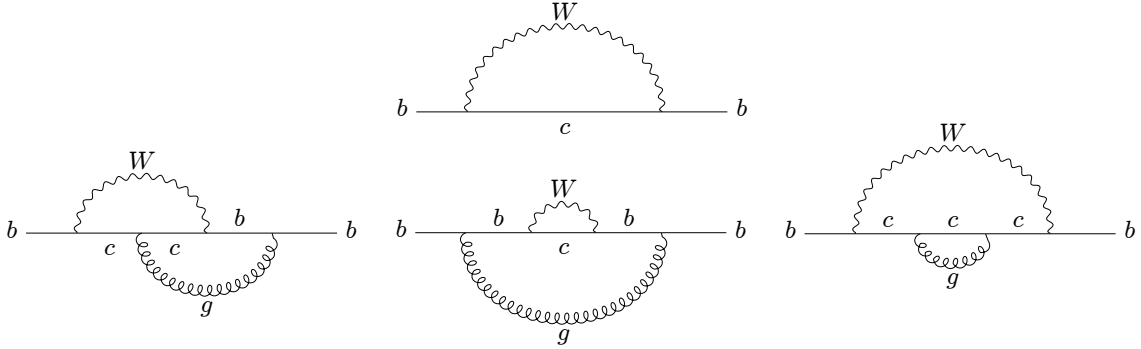


Figure 2: Feynman diagrams contributing to $\tilde{\Gamma}$ at the LO in QCD (top) and the NLO in QCD (bottom). At the NLO, the SIs were IBP-reduced to MIs belonging to the topology inherited from the first diagram in the bottom row.

The replacement of the lepton pair with an auxiliary light vector boson, schematically shown in figure 1, has already been applied in previous calculations of the q^2 spectrum — see, e.g., eq. (1)⁵ of ref. [19]. It serves two purposes. First, it allows for a straightforward use of the optical theorem while retaining the q^2 dependence of the spectrum in the vector-boson mass. If one would proceed with the calculation with the leptons, this dependence would be lost when the matrix element is integrated over all final states. To prevent this, one could use the equivalent method of reverse unitarity [20], but the effective width formula derived above proves to be easier to implement in practice. An additional benefit is that the lepton loop is evaluated automatically. With these two simplifications, to obtain the q^2 spectrum including the $\mathcal{O}(\alpha_s^n)$ correction, one has to calculate the imaginary parts of $(n + 1)$ -loop diagrams with 3 independent mass scales: m_b , m_c , and $\sqrt{q^2}$.

2.3 Calculation of the bare effective width

We compute the auxiliary width $\tilde{\Gamma}$ using the optical theorem

$$\tilde{\Gamma} = \frac{1}{2} \frac{1}{2m_b} 2\Im \left[-i \left(\sum_{\sigma_b} b \text{---} \text{---} \text{---} b \right) \right]. \quad (2.14)$$

Before turning to the calculation of $\mathcal{O}(\alpha_s^2)$ terms, we used eq. (2.13) to compute the known Leading Order (LO) q^2 spectrum, and the Next-to-LO (NLO) QCD correction. We generated the necessary b -propagator diagrams using **QGRAF** [21], and obtained the resulting algebraic expressions using a custom **Mathematica** code. The LO and NLO diagrams are shown in figure 2. Next, we expressed the contribution of each diagram to the amplitude as a linear combination of Scalar Integrals (SIs). They were reduced to a set of Master Integrals (MIs) using Integration-By-Parts (IBP) identities implemented in **KIRA** [22, 23]. Both at the LO and NLO in QCD, the SIs were reduced to MIs from single topologies. For the evaluation of the MIs at the LO and NLO, we utilized the Differential Equations (DEs) in the canonical form method with the help of the **Mathematica** package **LIBRA** [24], and expressed the resulting Goncharov polylogarithms as dilogarithms. The boundary conditions

⁵An extra factor of q^2/M_W^2 there w.r.t. our eq. (2.13) is due to different notational conventions.

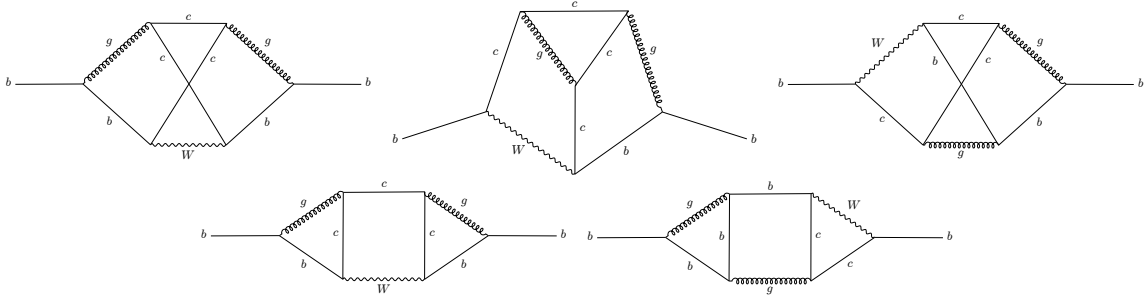


Figure 3: Sample diagrams contributing to $\tilde{\Gamma}$ at the NNLO in QCD. All SIs at this order were IBP-reduced to MIs from topologies inherited from the displayed five diagrams.

for the DEs were determined numerically using the auxiliary mass flow method [25, 26], implemented in the `Mathematica` package `AMFlow` [27]. Next, they were reconstructed as combinations of integers and π^2 using the `Mathematica` implementation of the PSLQ algorithm.

At the Next-to-NLO (NNLO), we identified 39 bare diagrams, with some examples shown in figure 3. We proceeded with the same method as at lower orders, performing IBP reductions of all SIs to obtain 98 MIs belonging to five different topologies. However, contrary to our approach at the LO and NLO, we did not use the DE method to evaluate them. Instead, we computed all the NNLO MIs using `AMFlow` at 682 different points in the $(q^2/m_b^2, m_c^2/m_b^2) \equiv (\hat{q}^2, \hat{m}_c^2)$ space, obtaining a dense scan of the bare part of $\tilde{\Gamma}$.

2.4 Renormalization

The bare part of $\tilde{\Gamma}$ has been computed using the dimensional regularization method in $D \equiv 4 - 2\epsilon$ dimensions. After taking the imaginary part of the MIs, the LO contribution is finite, the NLO correction has only a simple ϵ pole, and at the NNLO in QCD there are at most $1/\epsilon^2$ divergences. Not all of these divergences are purely ultraviolet, even though the quantity we consider is infrared- and collinear-safe. To arrive at the finite result, we perform the standard renormalization. We renormalize the quark fields and masses in the on-shell scheme, and use α_s in the $\overline{\text{MS}}$ scheme with five active flavours.

The renormalized $\tilde{\Gamma}$ is obtained by combining the bare and counterterm contributions as follows:

$$\tilde{\Gamma} = \lim_{\epsilon \rightarrow 0} \left[\tilde{\Gamma}^{\text{bare}} + \tilde{\Gamma}^{\otimes} \right] \equiv \lim_{\epsilon \rightarrow 0} \left[\sum_{n=0} \alpha_s^n \tilde{\Gamma}^{\text{bare}}(n) + \sum_{n=1} \alpha_s^n \tilde{\Gamma}^{\otimes}(n) \right]. \quad (2.15)$$

The individual contributions of one- and two-loop diagrams with counterterm insertions yield the following renormalization formulas:

$$\begin{aligned} \tilde{\Gamma}^{\otimes(1)} &= R_1^{(0)} \tilde{\Gamma}^{\text{bare}}(0), \\ \tilde{\Gamma}^{\otimes(2)} &= R_2^{(0)} \tilde{\Gamma}^{\text{bare}}(0) + R_2^{(1)} \tilde{\Gamma}^{\text{bare}}(1), \end{aligned} \quad (2.16)$$

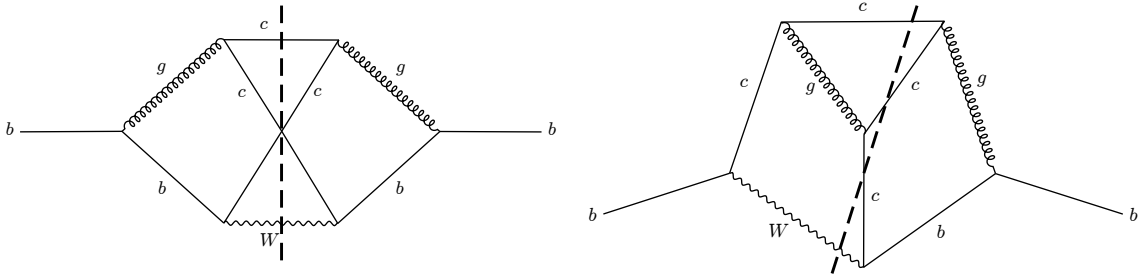


Figure 4: Two examples of cut diagrams contributing to the triple-charm channel. The dashed lines indicate unitarity cuts. All the 22 cut MIs in the triple-charm calculation belong to one of the two topologies inherited from the above diagrams.

where

$$\begin{aligned}
R_1^{(0)} &\equiv \delta_b^{(1)} + 2\delta_{m_c}^{(1)} \hat{m}_c^2 \partial_{\hat{m}_c^2}, \\
R_2^{(0)} &\equiv \delta_b^{(2)} + \left(2\delta_{m_c}^{(2)} + 2\delta_b^{(1)} \delta_{m_c}^{(1)} + \left(\delta_{m_c}^{(1)} \right)^2 \right) \hat{m}_c^2 \partial_{\hat{m}_c^2} + 2 \left(\delta_{m_c}^{(1)} \right)^2 \hat{m}_c^4 \partial_{\hat{m}_c^2}^2, \\
R_2^{(1)} &\equiv R_1^{(0)} + 2\delta_g^{(1)} + 2\delta_{m_b}^{(1)} m_b^2 \partial_{\tilde{m}_b^2} \Big|_{\tilde{m}_b = m_b},
\end{aligned} \tag{2.17}$$

and

$$\delta_a \equiv Z_a - 1 \equiv \alpha_s \delta_a^{(1)} + \alpha_s^2 \delta_a^{(2)} + \mathcal{O}(\alpha_s^3). \tag{2.18}$$

The necessary renormalization constants Z_a with $a = g, m_c, m_b$ can be found in refs. [28–30]. In the definition of $R_2^{(1)}$, the mass \tilde{m}_b should be inserted into the internal b -quark propagators when constructing seeds to perform the IBP reduction for the SIs, shifting the diagrams away from the on-shell relation $p_b^2 = m_b^2 \neq \tilde{m}_b^2$. After taking the partial derivative w.r.t. \tilde{m}_b^2 , the b -quark mass can be put back equal to $\sqrt{p_b^2}$, prior to the IBP reduction.

3 Results

3.1 The $b \rightarrow X_{3c} l \bar{\nu}_l$ spectrum

Once the renormalized $\tilde{\Gamma}$ has been computed, we can use the 4-dimensional relation (2.13) to get the semileptonic q^2 spectrum. The present subsection is devoted to the triple-charm $b \rightarrow X_{3c} l \bar{\nu}_l$ partonic channel. In the corresponding hadronic decay of the B -meson, the lightest possible hadronic final states have masses of order $m_D m_{\eta_c} \simeq 4.8 \text{ GeV}$, which differs from $m_B \simeq 5.3 \text{ GeV}$ only by $\mathcal{O}(\bar{\Lambda})$. Consequently, application of the $\bar{\Lambda}/m_b$ expansion as in eq. (1.1) becomes questionable. We have therefore decided to separate the $b \rightarrow X_{3c} l \bar{\nu}_l$ contribution from the better controlled single-charm $b \rightarrow X_{1c} l \bar{\nu}_l$ channel, both in the fit to the spectrum and to the moments. Such a separation also facilitates a direct comparison with the results of ref. [13].

As we are interested in the exclusive partonic $b \rightarrow cc\bar{l}\bar{\nu}_l$ decay channel, we have to consider diagrams with unitary cuts. Out of all 3-loop MIs present in the fully inclusive calculation, we extracted those with an allowed cut across three c -quark lines. This resulted

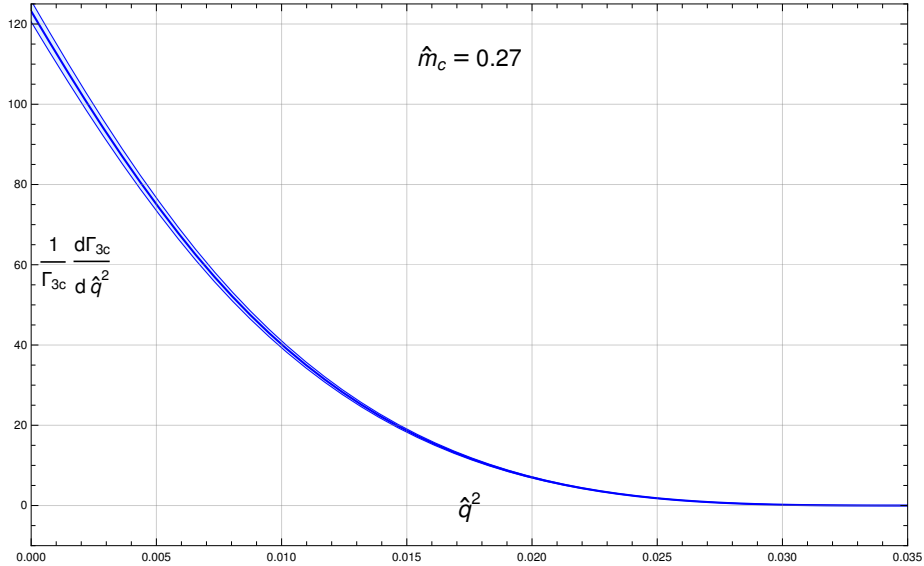


Figure 5: The \hat{q}^2 spectrum of the $b \rightarrow cc\bar{l}\bar{\nu}_l$ decay normalized to the width of this channel.

in 22 MIs belonging to 2 topologies shown in figure 4. We computed them using **AMFlow** at 650 points in the (\hat{q}^2, \hat{m}_c) space, with the following boundaries: $\hat{m}_c = 0.14$, $\hat{m}_c = 0.29$, $\hat{q}^2 = 0$, and $\hat{q}^2 = (1 - 3\hat{m}_c)^2$. The last boundary represents the largest kinematically allowed q^2 for the triple-charm semileptonic decay. We obtain the numerical results for the q^2 spectrum of the $b \rightarrow X_{3c}l\bar{\nu}_l$ channel width $\Gamma_{sl}^{\text{part},3c}$ with 60 significant digits. We then fit these results to the following ansatz:

$$\frac{d\Gamma_{sl}^{\text{part},3c}}{dq^2} = \alpha_s^2 m_b^3 G_F^2 |V_{cb}|^2 L_{3c}^{\frac{7}{2}} \left[\sum_{kl} C_{kl} \hat{q}^{2k} \hat{m}_c^l + \Theta[10L_{3c} - 1] \sum_{mn} \tilde{C}_{mn} \hat{q}^{2m} \hat{m}_c^n \right] + \mathcal{O}(\alpha_s^3), \quad (3.1)$$

where $L_{3c} \equiv (\hat{q}^2 - (1 + 3\hat{m}_c)^2)(\hat{q}^2 - (1 - 3\hat{m}_c)^2)$, and the ranges of indices k , l , m , and n are $(0, 2)$, $(0, 6)$, $(0, 4)$, and $(0, 6)$ respectively. The values of fit parameters C_{kl} and \tilde{C}_{mn} are listed in appendix A, tables 1 and 2, respectively. The relative error of this ansatz when compared with the results obtained using **AMFlow** is less than 1.5% for all points in the (\hat{q}^2, \hat{m}_c) space for which we performed the numerical calculation. The normalized spectrum of the $b \rightarrow cc\bar{l}\bar{\nu}_l$ channel is shown in figure 5. The indicated uncertainty comes entirely from the fitting error, as the renormalization scale dependence cancels out in the normalized spectrum. This uncertainty has been conservatively estimated by assuming a 1.5% error over the entire fit range. In reality, the uncertainty only reaches 1.5% at the extreme edge of the triple-charm phase space where the differential decay rate is strongly suppressed for kinematical reasons.

3.2 The $b \rightarrow X_{1c}l\bar{\nu}_l$ spectrum

The dominant part of the inclusive partonic width comes from the $b \rightarrow X_{1c}l\bar{\nu}_l$ channel. The ratio of widths of the single- and triple-charm channels as a function of \hat{m}_c is shown in figure 6. The indicated theoretical uncertainty has been estimated by varying the renor-

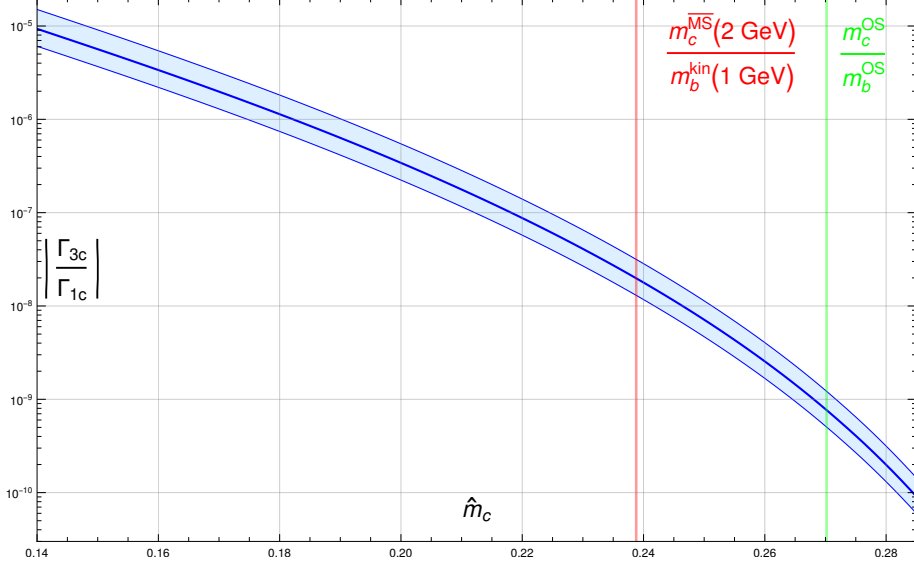


Figure 6: The ratio of the widths of the $b \rightarrow X_{3c} l \bar{\nu}_l$ and $b \rightarrow X_{1c} l \bar{\nu}_l$ channels. The red vertical line indicates the ratio of the $\overline{\text{MS}}$ charm mass renormalized at 2 GeV and the kinetic bottom mass with the separation scale of 1 GeV [12]. Our reference value of the on-shell mass ratio is indicated with the green vertical line.

malization scale between 2.3 GeV and 9.2 GeV. The uncertainty of the fits in this ratio is negligible.

We compute the NNLO QCD correction to the q^2 spectrum of the $b \rightarrow X_{1c} l \bar{\nu}_l$ channel by subtracting the triple-charm contribution described in the previous subsection from the fully inclusive correction obtained as a combination of the imaginary parts of the 98 MIs without cuts

$$\frac{d\Gamma_{sl}^{\text{part},1c(2)}}{dq^2} = \frac{d\Gamma_{sl}^{\text{part},(2)}}{dq^2} - \frac{d\Gamma_{sl}^{\text{part},3c(2)}}{dq^2}. \quad (3.2)$$

The above subtraction is performed for numerical results obtained with **AMFlow** with the precision of 60 significant digits at 682 points in the (\hat{q}^2, \hat{m}_c) parameter space, out of which 311 points satisfied the $\hat{q}^2 < (1 - 3\hat{m}_c)^2$ condition for a non-vanishing triple-charm part.

Using these numerical values for the $\mathcal{O}(\alpha_s^2)$ correction to the single-charm q^2 spectrum, we perform a fit using the following ansatz:

$$\frac{d\Gamma_{sl}^{\text{part},1c(2)}}{dq^2} = m_b^3 G_F^2 |V_{cb}|^2 L_{1c} \sum_{jkl} D_{jkl} \hat{m}_c^j \hat{q}^{2k} \log^l L_{1c}, \quad (3.3)$$

where $L_{1c} \equiv (\hat{q}^2 - (1 + \hat{m}_c)^2) (\hat{q}^2 - (1 - \hat{m}_c)^2)$, and the ranges of indices j , k , and l are (0, 1), (0, 7), and (0, 8) respectively. The fit coefficients D_{jkl} are presented in appendix A, in tables 3, 4, 5, and 6.

The results of the fit were compared with the analytic results presented in ref. [13] for 13600 points, as well as with the numerical values calculated using the method described above. The relative error never exceeded 5.2×10^{-4} . The q^2 spectrum of the single-charm

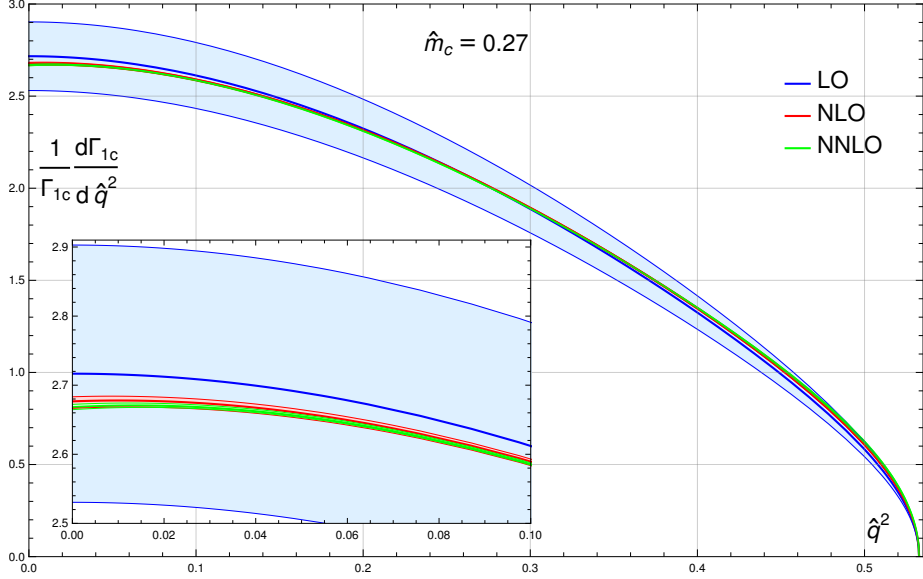


Figure 7: The \hat{q}^2 spectrum of the $b \rightarrow X_{1c} l \bar{\nu}_l$ decay normalized to the width of this channel. The bottom-left panel is the enlarged part of the spectrum close to $\hat{q}^2 = 0$.

channel, including the $\mathcal{O}(\alpha_s^2)$ correction is shown in figure 7. We observe a significant improvement in the behaviour of the perturbative series for the normalized spectrum, as compared to the unnormalized one. It suggests that a portion of the renormalon ambiguity is mitigated when the overall factor of $(m_b^{\text{OS}})^5$ cancels out. The uncertainty of the LO is estimated by assuming that $\text{NLO} \approx \text{LO} \alpha_s/\pi$. The uncertainties at the NLO and NNLO are obtained by varying the renormalization scale in the same range as in figure 6.

3.3 Corrections to the q^2 -moments

Values of the leptonic invariant mass in the semileptonic B meson decay can only be measured in bins of non-zero width. To compare these measurements directly with theoretical predictions, one would need to integrate the q^2 spectrum over the corresponding intervals. The HQE for such integrals is generally not well-behaved, especially near the maximal allowed q^2 . The extraction of $|V_{cb}|$, the quark masses, and non-perturbative matrix elements is instead performed by comparing theoretical predictions and measurements for moments of the spectrum.

Focusing on the partonic approximation, let us define the n -th q^2 moment of the semileptonic decay with a lower cut \hat{q}_{cut}^2 as

$$\hat{M}_n(\hat{q}_{\text{cut}}^2) \equiv \int_{\hat{q}_{\text{cut}}^2}^{(1-\hat{m}_c)^2} d\hat{q}^2 \hat{q}^{2n} \frac{d\Gamma_{sl}^{\text{part}}}{d\hat{q}^2}. \quad (3.4)$$

In the literature, $M_n = m_b^{2n} \hat{M}_n$ are often used instead. We shall also consider normalized

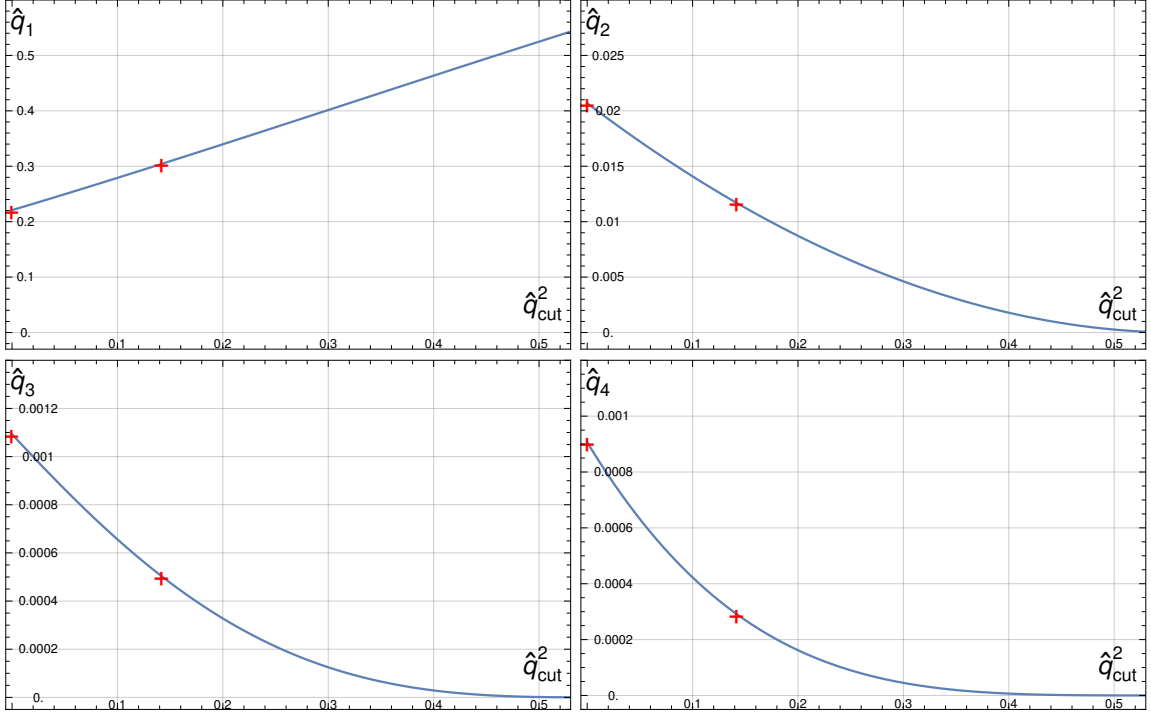


Figure 8: The first four centralized q^2 moments as functions of q_{cut}^2 for $\hat{m}_c = 0.25$. With red crosses, we indicate the numerical results given in eqs. (21) and (22) of ref. [13].

moments given by

$$\langle \hat{q}^{2n} \rangle_{\hat{q}^2 > \hat{q}_{cut}^2} \equiv \frac{\hat{M}_n(\hat{q}_{cut}^2)}{\hat{M}_0(\hat{q}_{cut}^2)}. \quad (3.5)$$

Finally, following ref. [31], we adopt the following definition for the centralized moments:

$$\begin{aligned} \hat{q}_1(\hat{q}_{cut}^2) &\equiv \langle \hat{q}^2 \rangle_{\hat{q}^2 > \hat{q}_{cut}^2}, \\ \hat{q}_n(\hat{q}_{cut}^2) &\equiv \langle (\hat{q}^2 - \langle \hat{q}^2 \rangle)^n \rangle_{\hat{q}^2 > \hat{q}_{cut}^2} = \\ &= \sum_{j=0}^n \binom{n}{j} \langle \hat{q}^{2j} \rangle_{\hat{q}^2 > \hat{q}_{cut}^2} (-\langle \hat{q}^2 \rangle_{\hat{q}^2 > \hat{q}_{cut}^2})^{n-j}. \end{aligned} \quad (3.6)$$

In figure 8, we show our results for the first four centralized moments in the on-shell scheme as functions of \hat{q}_{cut}^2 with the value of \hat{m}_c set to 0.25. To have a direct comparison with ref. [13], the presented centralized moments were calculated including only the single-charm NNLO QCD correction (3.3), and neglecting the triple-charm channel. With red crosses, we indicate the numerical results given in eqs. (21) and (22) of ref. [13]. We find exact agreement to all digits given in that publication.

Figure 9 depicts the relative impact of the triple-charm channel on the centralized moments when compared with the pure single-charm approximation, including the $\mathcal{O}(\alpha_s^3)$ correction. We define $\Delta \hat{q}_n^{3c}$ as

$$\Delta \hat{q}_n^{3c} \equiv \hat{q}_n - \hat{q}_n^{1c}, \quad (3.7)$$

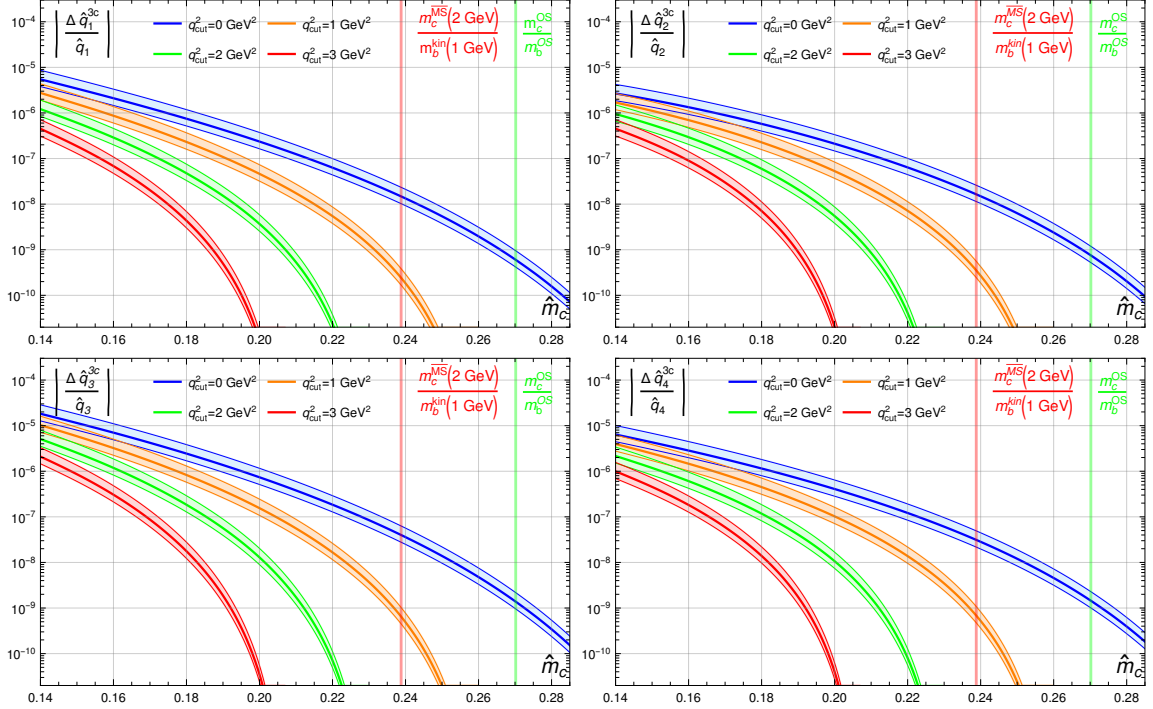


Figure 9: Relative impact of the triple-charm channel on the centralized q^2 moments as a function of \hat{m}_c and \hat{q}_{cut}^2 . For the definition of $\Delta\hat{q}_1^{3c}$ see the text. The red and green vertical lines indicate the same quark mass ratios as in figure 6.

where \hat{q}_n^{1c} is the centralized moment computed up to the NNLO QCD without including the triple-charm contribution. The above definition can naturally be interpreted as the error of the single-charm approximation. It decreases rapidly with increasing \hat{m}_c and \hat{q}_{cut}^2 , and for physical values of quark masses and non-zero q^2 cuts it quickly becomes negligible.

For comparison, in figure 10, we present the impact of the single-charm NNLO QCD term on the centralized q^2 moments. The difference $\Delta\hat{q}_n^{1c}$ is defined as

$$\Delta\hat{q}_n^{1c} \equiv \hat{q}_n^{1c} - \hat{q}_n^{\text{NLO}}, \quad (3.8)$$

where \hat{q}_n^{NLO} is the moment computed at the NLO only.

4 Conclusions

The recent focus of both the theoretical and experimental communities in the area of inclusive semileptonic decays of the B meson stems from the need for improving the precision of $|V_{cb}|$ determination in the SM. The measurements of q^2 moments by Belle and Belle II, along with calculations of various perturbative and non-perturbative effects allow to significantly enhance the precision of extracting $|V_{cb}|$ and non-perturbative matrix elements. This, in turn, narrows down the uncertainty of the SM predictions for other phenomenologically important observables. The present paper contributes to these efforts in two ways. First, it provides an independent verification of the NNLO single-charm contribution to the

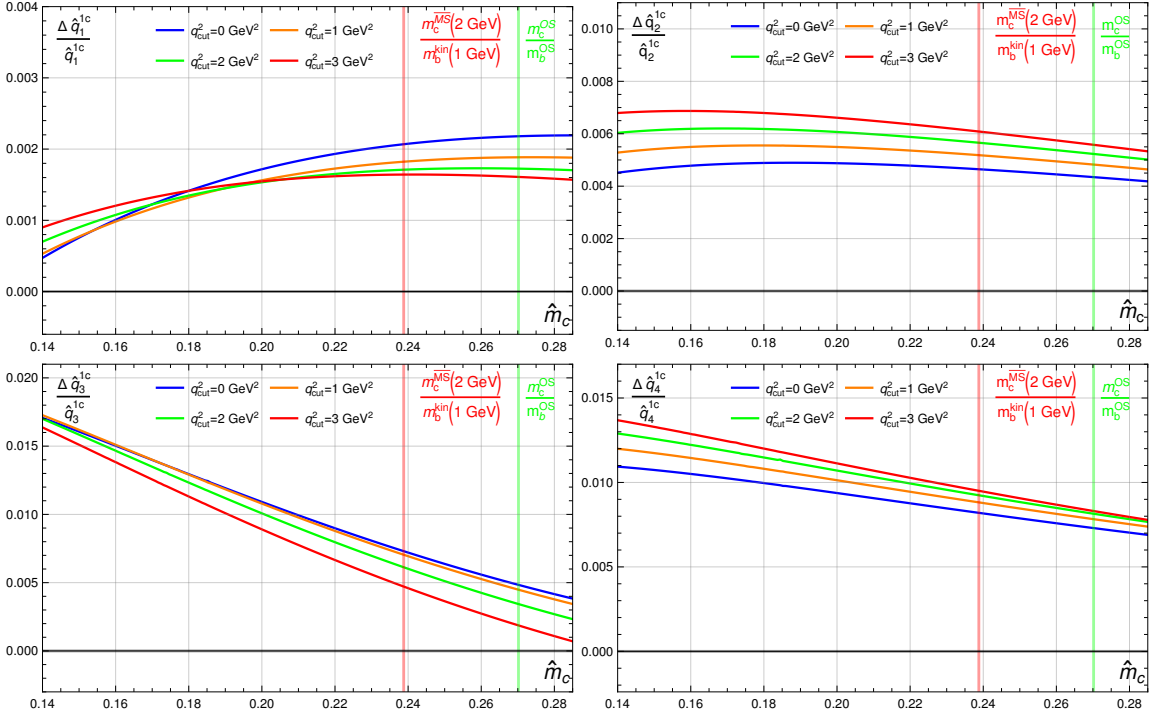


Figure 10: Relative impact of the single-charm NNLO QCD correction on the centralized q^2 moments as a function of \hat{m}_c and \hat{q}_{cut}^2 . For the definition of $\Delta \hat{q}_i^{1c}$ see the text. For clarity, we omit uncertainties from varying the renormalization scale.

partonic q^2 spectrum, recently evaluated in ref. [13]. Second, it extends this calculation by incorporating effects of the $b \rightarrow cc\bar{c}l\bar{\nu}_l$ decay channel. Our analysis made extensive use of the auxiliary mass flow method, implemented in the **AMFlow** package. The precise numerical results obtained with this tool were used to perform fits to the single- and triple-charm channel contributions to the q^2 spectrum, which we have provided in the ancillary files. In addition to studying the q^2 spectrum itself, we analyzed the impact of the triple-charm channel on the centralized q^2 moments of the spectrum, comparing it with the dominant single-charm NNLO QCD correction. We confirm that for the physical values of quark masses and for cuts on low q^2 employed in contemporary experiments, the impact of the triple-charm channel is minuscule. Nevertheless, our calculation provides the first fully quantitative analysis of this channel.

Acknowledgments

We would like to thank Matteo Fael, Paolo Gambino and Matthias Steinhauser for useful discussions. This work was supported in part by the National Science Center, Poland, under the research projects 2020/37/B/ST2/02746 (all the authors) and 2023/49/B/ST2/00856 (MM only).

A Numerical values of fit parameters

In this appendix, we present numerical values of the fit coefficients for the single-charm fit, as given in eq. (3.3), and the triple-charm fit, as given in eq. (3.1). The complete expressions for the fits are available in the ancillary file.

C_{kl}	$k = 0$	$k = 1$	$k = 2$
$l = 0$	-0.000862940	-0.001237605	-0.002930817
$l = 1$	0.022083312	0.058729219	0.115555544
$l = 2$	-0.233051560	-0.929611726	-1.948951905
$l = 3$	1.300169847	7.064296877	17.168143423
$l = 4$	-4.046951098	-28.327414394	-82.170972154
$l = 5$	6.666415074	57.939616602	202.387552617
$l = 6$	-4.541480275	-47.726627340	-200.982999303

Table 1: Coefficients C_{kl} of the triple-charm fit (3.1).

\tilde{C}_{mn}	$m = 0$	$m = 1$	$m = 2$	$m = 3$	$m = 4$
$n = 0$	0.000877518	0.001621422	0.003642739	0.004746374	0.640253858
$n = 1$	-0.022328502	-0.068057724	-0.138426420	-0.028111942	-20.337500422
$n = 2$	0.234808565	1.020865993	2.251801608	-1.305831462	258.079023134
$n = 3$	-1.306653472	-7.508277813	-19.200975797	19.197488356	-1635.101572743
$n = 4$	4.059050049	29.397188800	88.978406754	-95.971405644	5172.363417944
$n = 5$	-6.675376047	-58.957345285	-211.538554968	167.311712182	-6539.450493870
$n = 6$	4.541480275	47.726627340	200.982999303	0	0

Table 2: Coefficients \tilde{C}_{mn} of the triple-charm fit (3.1).

D_{0kl}	$k = 0$	$k = 1$	$k = 2$	$k = 3$
$l = 0$	-0.00065492620361	-0.00390985766592	-0.00220565766436	0.15518605570268
$l = 1$	-0.00142837487165	0.00696508473371	0.09405910531312	-0.06253133578189
$l = 2$	0.00315708546717	-0.02325332865210	0.00374231943691	-2.02104356689117
$l = 3$	-0.01566245331197	0.00539313247413	-0.16514145943056	0.50368450565789
$l = 4$	-0.00314430463123	0.03298251534973	-0.24771235141673	0.79272863991011
$l = 5$	-0.00116367410900	-0.00066823342187	-0.01632951298570	0.12789891805598
$l = 6$	-0.00016427141654	-0.00086937186633	0.00406718033696	0.00295240291003
$l = 7$	-0.00002838003168	-0.00013193918044	0.00091118101557	-0.00127493558773
$l = 8$	-0.00000311384087	-0.00000605460509	0.00008807454959	-0.00020743224743

Table 3: Coefficients D_{0kl} of the single-charm fit (3.3) for k between 0 and 3.

D_{0kl}	$k = 4$	$k = 5$	$k = 6$	$k = 7$
$l = 0$	-0.08570516624642	-2.60307981382978	5.46598388371161	-3.07155763105516
$l = 1$	-4.45202557105393	12.27898482822888	-12.17665279523761	4.05283421170514
$l = 2$	6.82900780658794	-8.98001675918627	4.79587351688384	-0.71420622887211
$l = 3$	-0.22696886297429	-0.79009467604488	0.80044056001754	-0.12969467182270
$l = 4$	-1.19412096570063	0.75616420973758	-0.12462741476560	-0.01366414279716
$l = 5$	-0.29957244184153	0.30137080814560	-0.13593627512955	0.02437018661001
$l = 6$	-0.03090584845561	0.04725296326283	-0.02906154255314	0.00673101795849
$l = 7$	-0.00087783536997	0.00342046404978	-0.00276819278253	0.00074981715535
$l = 8$	0.00013718255663	0.00010589907564	-0.00017873779555	0.00006418583561

Table 4: Coefficients D_{0kl} of the single-charm fit (3.3) for k between 4 and 7.

D_{1kl}	$k = 0$	$k = 1$	$k = 2$	$k = 3$
$l = 0$	0.00037898651589	0.00517918021788	0.04112085070528	-0.21496054486301
$l = 1$	0.00294905480007	-0.00603971843699	-0.21895793674020	-1.03193199304427
$l = 2$	-0.01351315180078	-0.01995812054357	-0.22812429086629	3.41257368948131
$l = 3$	0.01475940605979	0.00798442052509	0.20625870040905	-0.22965190841787
$l = 4$	0.00361472380470	-0.04512665323742	0.27522405293211	-0.58912224362215
$l = 5$	0.00135041781442	0.00257101526830	0.03190378201141	-0.15565929828791
$l = 6$	0.00018496716551	0.00151028010054	-0.00216460072286	-0.01607688792361
$l = 7$	0.00003136294993	0.00026420915586	-0.00084445521789	-0.00038980944792
$l = 8$	0.00000345408063	0.00001942254381	-0.00010722136685	0.00009668851788

Table 5: Coefficients D_{1kl} of the single-charm fit (3.3) for k between 0 and 3.

D_{1kl}	$k = 4$	$k = 5$	$k = 6$	$k = 7$
$l = 0$	-1.01037416347829	3.85777242049678	-4.82260835024637	2.43237146133600
$l = 1$	7.28407942435662	-11.41492712861138	3.15489853106631	4.33118652047488
$l = 2$	-6.95529309256300	2.97749311540542	2.87779195568835	-0.44612980575120
$l = 3$	-0.81288724990409	1.05952773710921	0.58597841341702	-0.21167555956766
$l = 4$	0.25138154880765	0.49282349653529	-0.24333580413142	0.01386846240050
$l = 5$	0.20204027536542	-0.02532694776417	-0.04866750001498	0.01886365093423
$l = 6$	0.04112674519580	-0.02440884452889	-0.00083229803405	0.00359648817752
$l = 7$	0.00367275991399	-0.00340746780997	0.00055454715801	0.00030764562717
$l = 8$	0.00017167412681	-0.00029973464715	0.00010242601552	0.00001903450238

Table 6: Coefficients D_{1kl} of the single-charm fit (3.3) for k between 4 and 7.

References

- [1] M. Czaja and M. Misiak, “Current Status of the Standard Model Prediction for the $B_s \rightarrow \mu^+ \mu^-$ Branching Ratio,” *Symmetry* **16** (2024) no.7, 917 doi:10.3390/sym16070917 [arXiv:2407.03810 [hep-ph]].
- [2] S. Jwa, J. Kim, S. Kim, S. Lee, W. Lee, J. Leem, J. Pak and S. Park, “2023 update of ε_K with lattice QCD inputs,” *PoS LATTICE2023* (2024), 160 doi:10.22323/1.453.0160 [arXiv:2312.02986 [hep-lat]].
- [3] A. Alberti, P. Gambino, K. J. Healey and S. Nandi, “Precision Determination of the

- Cabibbo-Kobayashi-Maskawa Element V_{cb} ,* Phys. Rev. Lett. **114** (2015) no.6, 061802 doi:10.1103/PhysRevLett.114.061802 [arXiv:1411.6560 [hep-ph]].
- [4] A. J. Bevan *et al.* [BaBar and Belle], “*The Physics of the B Factories,*” Eur. Phys. J. C **74** (2014), 3026 doi:10.1140/epjc/s10052-014-3026-9 [arXiv:1406.6311 [hep-ex]].
- [5] R. van Tonder *et al.* [Belle], “*Measurements of q^2 Moments of Inclusive $B \rightarrow X_c \ell^+ \nu_\ell$ Decays with Hadronic Tagging,*” Phys. Rev. D **104** (2021) no.11, 112011 doi:10.1103/PhysRevD.104.112011 [arXiv:2109.01685 [hep-ex]].
- [6] F. Abudinén *et al.* [Belle-II], “*Measurement of lepton mass squared moments in $B \rightarrow X_c \ell \bar{\nu}_\ell$ decays with the Belle II experiment,*” Phys. Rev. D **107** (2023) no.7, 072002 doi:10.1103/PhysRevD.107.072002 [arXiv:2205.06372 [hep-ex]].
- [7] A. V. Manohar and M. B. Wise, “*Heavy quark physics,*” Camb. Monogr. Part. Phys. Nucl. Phys. Cosmol. **10** (2000), 1-191.
- [8] D. M. Webber *et al.* [MuLan], “*Measurement of the Positive Muon Lifetime and Determination of the Fermi Constant to Part-per-Million Precision,*” Phys. Rev. Lett. **106** (2011), 041803 doi:10.1103/PhysRevLett.106.079901 [arXiv:1010.0991 [hep-ex]].
- [9] T. Mannel, D. Moreno and A. A. Pivovarov, “*NLO QCD corrections to inclusive $b \rightarrow c \ell \bar{\nu}$ decay spectra up to $1/m_Q^3$,*” Phys. Rev. D **105** (2022) no.5, 054033 doi:10.1103/PhysRevD.105.054033 [arXiv:2112.03875 [hep-ph]].
- [10] T. Mannel and K. K. Vos, “*Reparametrization Invariance and Partial Re-Summations of the Heavy Quark Expansion,*” JHEP **06** (2018), 115 doi:10.1007/JHEP06(2018)115 [arXiv:1802.09409 [hep-ph]].
- [11] F. Bernlochner, M. Fael, K. Olschewsky, E. Persson, R. van Tonder, K. K. Vos and M. Welsch, “*First extraction of inclusive V_{cb} from q^2 moments,*” JHEP **10** (2022), 068 doi:10.1007/JHEP10(2022)068 [arXiv:2205.10274 [hep-ph]].
- [12] G. Finauri and P. Gambino, “*The q^2 moments in inclusive semileptonic B decays,*” JHEP **02** (2024), 206 doi:10.1007/JHEP02(2024)206 [arXiv:2310.20324 [hep-ph]].
- [13] M. Fael and F. Herren, “*NNLO QCD corrections to the q^2 spectrum of inclusive semileptonic B-meson decays,*” JHEP **05** (2024), 287 doi:10.1007/JHEP05(2024)287 [arXiv:2403.03976 [hep-ph]].
- [14] A. Alberti, T. Ewerth, P. Gambino and S. Nandi, “*Kinetic operator effects in $\bar{B} \rightarrow X_c \ell \nu$ at $O(\alpha_s)$,*” Nucl. Phys. B **870** (2013), 16-29 doi:10.1016/j.nuclphysb.2013.01.005 [arXiv:1212.5082 [hep-ph]].
- [15] A. Alberti, P. Gambino and S. Nandi, “*Perturbative corrections to power suppressed effects in semileptonic B decays,*” JHEP **01** (2014), 147 doi:10.1007/JHEP01(2014)147 [arXiv:1311.7381 [hep-ph]].
- [16] M. Fael, K. Schönwald and M. Steinhauser, “*Third order corrections to the semileptonic $b \rightarrow c$ and the muon decays,*” Phys. Rev. D **104** (2021) no.1, 016003 doi:10.1103/PhysRevD.104.016003 [arXiv:2011.13654 [hep-ph]].
- [17] M. Fael, K. Schönwald and M. Steinhauser, “*A first glance to the kinematic moments of $B \rightarrow X_c \ell \nu$ at third order,*” JHEP **08** (2022), 039 doi:10.1007/JHEP08(2022)039 [arXiv:2205.03410 [hep-ph]].
- [18] V. Aquila, P. Gambino, G. Ridolfi and N. Uraltsev, “*Perturbative corrections to semileptonic*

- b* decay distributions,” Nucl. Phys. B **719** (2005), 77-102 doi:10.1016/j.nuclphysb.2005.04.031 [arXiv:hep-ph/0503083 [hep-ph]].
- [19] M. Dowling, A. Pak and A. Czarnecki, “*Semi-Leptonic b-decay at Intermediate Recoil*,” Phys. Rev. D **78** (2008), 074029 doi:10.1103/PhysRevD.78.074029 [arXiv:0809.0491 [hep-ph]].
- [20] C. Anastasiou and K. Melnikov, “*Higgs boson production at hadron colliders in NNLO QCD*,” Nucl. Phys. B **646** (2002), 220-256 doi:10.1016/S0550-3213(02)00837-4 [arXiv:hep-ph/0207004 [hep-ph]].
- [21] P. Nogueira, “*Automatic Feynman graph generation*,” J. Comput. Phys. **105** (1993), 279 doi:10.1006/jcph.1993.1074.
- [22] P. Maierhöfer, J. Usovitsch and P. Uwer, “*Kira—A Feynman integral reduction program*,” Comput. Phys. Commun. **230** (2018), 99-112 doi:10.1016/j.cpc.2018.04.012 [arXiv:1705.05610 [hep-ph]].
- [23] J. Klappert, F. Lange, P. Maierhöfer and J. Usovitsch, “*Integral reduction with Kira 2.0 and finite field methods*,” Comput. Phys. Commun. **266** (2021), 108024 doi:10.1016/j.cpc.2021.108024 [arXiv:2008.06494 [hep-ph]].
- [24] R. N. Lee, “*Libra: A package for transformation of differential systems for multiloop integrals*,” Comput. Phys. Commun. **267** (2021), 108058 doi:10.1016/j.cpc.2021.108058 [arXiv:2012.00279 [hep-ph]].
- [25] X. Liu, Y. Q. Ma and C. Y. Wang, “*A Systematic and Efficient Method to Compute Multi-loop Master Integrals*,” Phys. Lett. B **779** (2018), 353-357 doi:10.1016/j.physletb.2018.02.026 [arXiv:1711.09572 [hep-ph]].
- [26] X. Liu and Y. Q. Ma, “*Multiloop corrections for collider processes using auxiliary mass flow*,” Phys. Rev. D **105** (2022) no.5, L051503 doi:10.1103/PhysRevD.105.L051503 [arXiv:2107.01864 [hep-ph]].
- [27] X. Liu and Y. Q. Ma, “*AMFlow: A Mathematica package for Feynman integrals computation via auxiliary mass flow*,” Comput. Phys. Commun. **283** (2023), 108565 doi:10.1016/j.cpc.2022.108565 [arXiv:2201.11669 [hep-ph]].
- [28] D. J. Gross and F. Wilczek, “*Ultraviolet behavior of nonabelian gauge theories*,” Phys. Rev. Lett. **30** (1973), 1343-1346 doi:10.1103/PhysRevLett.30.1343.
- [29] K. Melnikov and T. van Ritbergen, “*The Three loop on-shell renormalization of QCD and QED*,” Nucl. Phys. B **591** (2000), 515-546 doi:10.1016/S0550-3213(00)00526-5 [arXiv:hep-ph/0005131 [hep-ph]].
- [30] S. Bekavac, A. Grozin, D. Seidel and M. Steinhauser, “*Light quark mass effects in the on-shell renormalization constants*,” JHEP **10** (2007), 006 doi:10.1088/1126-6708/2007/10/006 [arXiv:0708.1729 [hep-ph]].
- [31] M. Fael, T. Mannel and K. Keri Vos, “ *V_{cb} determination from inclusive $b \rightarrow c$ decays: an alternative method*,” JHEP **02** (2019), 177 doi:10.1007/JHEP02(2019)177 [arXiv:1812.07472 [hep-ph]].